

COVER PAGE

Document downloaded by @DAEL

Fri Nov 27 05:16:43 2026
For personal use

When automatic English translation is provided, only the original document is authentic.
The EAA cannot be held responsible of any translation error

Bibliographical reference

Focusing Ultrasonic Waves Using a Biconcave Lens: Normal Incidence on the Lens, Tomoo Kamakura, Kenichi Aoki and Toshiaki Nakamura, Acta Acustica **vol. 94** (Number 1), 2008, pp. 104-113

DOI
https://doi.org/10.3813/AAA.918013

ACTA ACUSTICA UNITED WITH ACUSTICA
Vol. 94 (2008) 104 – 113

DOI 10.3813/AAA.918013

Focusing Ultrasonic Waves Using a Biconcave Lens: Normal Incidence on the Lens

Tomoo Kamakura, Kenichi Aoki
The University of Electro-Communications, 1-5-1 Chofugaoka, Chofu-shi 182-8585, Japan.
kamakura@ee.uec.ac.jp

Toshiaki Nakamura
National Defense Academy, 1-10-20 Hashirimizu, Yokosuka-shi 239-8686, Japan

Summary
In this paper, we theoretically and experimentally investigated the focusing of plane progressive waves and directive beams using a spherically curved biconcave lens at normal incidence. The lens is made of acrylic resin or polymethylmethacrylate (PMMA) and is submerged in water. Our analytical approach is based on a classical theory that expands an incident wave into spherical waves to satisfy boundary conditions conveniently at the spherical interface between the water and the lens. The continuity conditions of displacement and stress at the interface determine the generation of longitudinal and shear waves in the lens. Additionally, sound absorption in the lens is considered. The Rayleigh integral associated with the particle velocity on the exit interface enables us to evaluate all sound fields behind the lens. Numerical examples demonstrate that no significant effect appears in the fields near the focus rather than in the pre-focal and post-focal regions even when the shear wave generation is included in the theory. To verify the usefulness of the present theory, we conducted experiments in water using a directive beam emitted from a 1-MHz circular-aperture transducer. It has been demonstrated that the agreement between the theory and the experiment is generally excellent.

PACS no. 43.20.Dk, 43.20.Gp, 43.58.Ls

1. Introduction

Acoustic lenses are widely used in ultrasonic-imaging systems to display high-spatial-resolution images and to allow ultrasounic equipment to reach high acoustic power at a focal point in industrial technology. Different from other beamformers such as an annular phased array, acoustic lenses have salient features in that they form readily focused beams with no circuitry and thus can dispense with complex electronics and its power assumption.

Incidentally, the geometric ray theory is used as a useful predictor like optics and provides a first approximation in evaluating lens performance. It is well known, however, that the ray model breaks down in principle near the focus, where wave diffraction becomes a significant factor in sound-field formation. Additionally, it does not consider the shear waves that may be excited at the interface between the lens and the surrounding fluid and may potentially affect the field profile. In contrast, wave acoustics can accurately analyze fields, even for mode conversion, although some tedious numerical computation is required. Recently, an alternative predictor or hybrid method that incorporates concepts of utilizing geometric acoustics in a lens and wave acoustics in an image space behind the final lens surface has been introduced to evaluate lens performance before fabrication in a sonar imaging system [1]. Actually, this hybrid method may be powerful in analyzing focused fields achieved by a single lens and a multilens system. Unfortunately, however, the effectiveness of the hybrid method has not been completely verified thus far from at least a theoretical viewpoint.

Aside from the hybrid method, we have developed a full wave theory for investigating sound focusing achieved by a spherically curved biconcave lens [2]. This analytical approach is based on a classical theory that expands an incident wave into spherical waves to be able to impose successfully boundary conditions at the spherical interface between the water and the lens.

The boundary conditions are the continuities of displacement and stress, determining the generation of not only longitudinal waves but also shear waves in the lens. To predict the focused field, the Rayleigh integral formula is used on the exit surface of the lens. Several researchers point out that mode conversion is relatively unimportant in lens performance [3, 4, 5]. They also insist that only negligible differences occur even if the presence of shear waves is accounted for, although their analyses still lack quantitative evaluation. Our numerical examples have demonstrated that sound-pressure profiles near the focus are less

Received 7 July 2006,
accepted 23 October 2007.

© S. Hirzel Verlag · EAA

affected by shear wave generation and supported that the opinion of the unimportance of shear wave generation is helpful in designing lenses [2].

Our main concern in this paper is to clarify the effectiveness of our wave theory through experiments in water. First, the theory is summarized with some numerical examples of focused fields achieved by a biconcave acoustic lens. Second, the experimental setup employed is described. We prepare two spherically biconcave lenses made of polymethylmethacrylate (PMMA). One lens has the same 60-mm curvature radius on the inlet and exit surfaces. The other lens has the radii of 100 mm and 35.5 mm. The focal lengths of both lenses are nearly identical. The sound source used is a 1-MHz planar transducer with a circular aperture of 9.5 mm radius. Each lens is located at 45 cm away from the source due to the limited dimensions of a water tank. Sound pressure distributions along and across the beam axis are then precisely measured using a miniature hydrophone and a reliable translation stage.

As a matter of fact, the lens location does not correspond to the farfield region where the experimental environment of plane wave propagation is realized. We have already reported that the focal length measured for a directive wave is considerably different from the theoretical focal length for a plane wave [6]. Therefore, it is of great importance that the theory is modified on the basis of the actual situation of the incidence of directive beams on the lens. The theoretical predictions thus obtained are compared carefully with experimental data.

Finally, the present paper presents the discussion of the applicability of the hybrid method to the present lens model. Although numerical demonstrations are limited to a single lens and a normal incident case, it is revealed that the hybrid method is a crude predictor for describing sound propagation characteristics and an almost satisfactory predictor for describing beam patterns in the focal plane.

2. Theory

Referring to the previous paper [2], we summarize the theoretical analysis of focused fields achieved by a biconcave acoustic lens. Figure 1 shows an acoustic lens with two spherically concave interfaces, S_1 and S_2, between the lens and the water, with the curvature radii d_1 and d_2. For simplicity, we assume that there are no boundaries in the direction of the colatitude angle. The water is almost inviscid. Sound waves in the water are then governed by the lossless Helmholtz equation

$$\nabla^2\phi + k^2\phi = 0, \tag{1}$$

where ϕ is the velocity potential, $k = \omega/c$ is the wave number, and c is the sound speed. Since the lens is ordinarily made of solid material, both longitudinal and shear waves may be generated at the inlet interface S_1. The particle displacement $\boldsymbol{u}$ for such elastic waves satisfies

$$\boldsymbol{u} = \nabla\psi + \nabla \times \boldsymbol{A}, \tag{2}$$

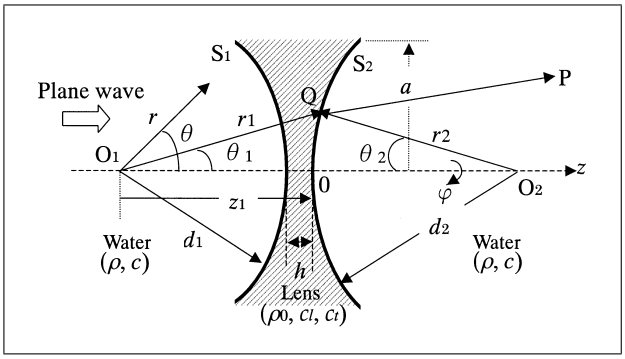

Figure 1. Theoretical model of a biconcave acoustic lens.

$$\nabla^2\psi + k_l^2\psi = 0 \quad (k_l = \omega/c_l), \tag{3}$$

$$\nabla \times \nabla \times \boldsymbol{A} - k_t^2\boldsymbol{A} = 0 \quad (k_t = \omega/c_t), \tag{4}$$

where ψ is the scalar potential and $\boldsymbol{A}$ is the vector potential. The sound speed of the longitudinal wave is $c_l = \sqrt{(\lambda + 2\mu)/\rho_0}$ and $c_t = \sqrt{\mu/\rho_0}$ is the speed of the shear wave. In the expressions of the two speeds, λ and μ are the Lamé constants, and ρ_0 is the lens density.

Let a plane acoustic wave of angular frequency ω be travelling parallel to the positive z axis and impinging normally on the lens. This incident wave ϕ_i with a unity amplitude is given by

$$\phi_i = \mathrm{e}^{-\mathrm{j}kz} = \mathrm{e}^{-\mathrm{j}kr\cos\theta}, \tag{5}$$

where r and θ are the spatial variables in the spherical coordinate system whose center is located at the origin O_1. The expansion of ϕ_i in terms of the eigenfunctions of equation (1) yields

$$\phi_i = \sum_{n=0}^{\infty}(-\mathrm{j})^n(2n+1)j_n(kr)P_n(\cos\theta), \tag{6}$$

where $j_n(\cdot)$ and $P_n(\cdot)$ are the spherical Bessel function and Legendre polynomial, respectively.

When the wave reaches the interface S_1 where the properties of the medium change abruptly, we can expect both the reflection and transmission of the wave to occur. The reflected or scattered wave ϕ_r is expanded into a similar series with coefficients A_n, which will be determined later by imposing appropriate boundary conditions.

$$\phi_r = \sum_{n=0}^{\infty} A_n(-\mathrm{j})^n(2n+1)h_n^{(1)}(kr)P_n(\cos\theta). \tag{7}$$

Here, $h_n^{(1)}(\cdot)$ is the spherical Hankel function of the first kind.

We can now solve equations (3) and (4). The displacement field in the lens is axisymmetric around the z axis, and the shear wave must fulfill the solenoidal condition of $\nabla\cdot\boldsymbol{A} = 0$. Therefore, $\boldsymbol{A}$ has only the component $A_\varphi(r, \theta)$ in the longitude-angle direction around the z axis. This leads to the scalar wave equation

$$\nabla^2 A_\varphi - \frac{A_\varphi}{r^2\sin^2\theta} + k_t^2 A_\varphi = 0. \tag{8}$$

By the same expansion as the solution of equation (7), the potentials ψ and A_φ must have solutions with the coefficients B_n and C_n as

$$\psi = \sum_{n=0}^{\infty} B_n(-\mathrm{j})^n(2n+1)h_n^{(2)}(k_l r)P_n(\cos\theta), \tag{9}$$

$$A_\varphi = \sum_{n=0}^{\infty} C_n(-\mathrm{j})^n(2n+1)h_n^{(2)}(k_t r)\frac{\mathrm{d}}{\mathrm{d}\theta}P_n(\cos\theta), \tag{10}$$

where $h_n^{(2)}(\cdot)$ is the spherical Hankel function of the second kind. From equation (2), we derive the displacement components u_r and u_θ from ψ and A_φ as

$$u_r = \frac{\psi}{\partial r} + \frac{1}{r\sin\theta}\frac{\partial}{\partial\theta}(\sin\theta A_\varphi), \tag{11}$$

$$u_\theta = \frac{1}{r}\frac{\psi}{\theta} - \frac{1}{r}\frac{\partial}{\partial r}\frac{\partial}{\partial r}(rA_\varphi). \tag{12}$$

The unknown coefficients A_n, B_n, and C_n are to be determined by applying three boundary conditions.

First, the radial component of the particle velocity must be continuous at the interface S_1, that is,

$$-\frac{\partial}{\partial r}(\phi_i + \phi_r) = \mathrm{j}\omega u_r \quad (\text{at } r = d_1). \tag{13}$$

For the colatitude component u_θ, there is no constraint because we neglect viscosity in the water. The second and third boundary conditions are given by the continuity of stress. The stress components related to the present lens model are T_{rr} and $T_{r\theta}$. They take the forms

$$T_{rr} = \lambda\Delta + 2\mu\frac{\partial u_r}{\partial r}, \tag{14}$$

$$T_{r\theta} = \mu\left(\frac{\partial u_\theta}{\partial r} - \frac{\partial u_\theta}{\partial r} + \frac{1}{r}\frac{\partial u_r}{\partial\theta}\right), \tag{15}$$

where $\Delta = \nabla\cdot\boldsymbol{u} = \nabla^2\psi = -k_l^2\psi$. Because the component T_{rr} is equal to the sound pressure at the interface S_1, the boundary condition becomes

$$\begin{aligned}-\mathrm{j}\omega\rho(\phi_i + \phi_r) &= \lambda\Delta + 2\mu\frac{\partial u_r}{\partial r}\\ &= -\lambda k_l^2\psi + 2\mu\frac{\partial u_r}{\partial r} \quad (\text{at } r = d_1),\end{aligned} \tag{16}$$

whereas the component $T_{r\theta}$ has to vanish. This leads to the remaining boundary condition

$$\frac{\partial u_\theta}{\partial r} - \frac{u_\theta}{r} + \frac{1}{r}\frac{\partial u_r}{\partial\theta} = 0 \quad (\text{at } r = d_1). \tag{17}$$

Thus, we can determine the coefficients A_n, B_n and C_n completely from the three boundary conditions in equations (13), (16), and (17), although some perseverance is required to derive solutions.

When waves travel through the lens and reach the exit interface S_2, they are partially reflected because the acoustic impedance of the lens differs from that of the fluid. The reflected waves travel back to the inlet surface, and wave reflection occurs again at the interface S_1. We may ignore such multiple reflections because the nonplanar configuration of the concave interfaces is likely to weaken the reflection.

Table I. Physical parameters and dimensions of a PMMA lens. The subscript "*l* " refers to longitudinal waves, and the subscript "*s* " refers to shear waves. The sound-absorption coefficients and speed are measured at 1 MHz and room temperature.

Lens density ρ_0 [kg/m^3]	1180
Sound velocity c_l [m/s]	2760
Sound velocity c_s [m/s]	1340
Absorption coefficient α_l [neper/m]	15
Absorption coefficient α_s [neper/m]	39
Water density ρ [kg/m^3]	998
Sound velocity c [m/s]	1483
Sound absorption	neglected
Curvature radius d_1 [mm]	60
Curvature radius d_2 [mm]	60
Thickness h [mm]	2
Aperture radius a [mm]	37.5

According to the Huygens-Fresnel principle, each point on the exit surface S_2 emits a secondary wavelet with an approprite amplitude and phase. To accomplish this formulation, we now introduce a simple expression for the normal component of the transmitted particle velocity on the interface S_2 as follows (see Appendix A):

$$v_n = \frac{2Z_l}{Z_w + Z_l}(\boldsymbol{v}\cdot\boldsymbol{n}). \tag{18}$$

Here, $\boldsymbol{v}$ is the particle velocity when the boundary S_2 is hypothetically absent and is expressed as

$$\boldsymbol{v} = \mathrm{j}\omega(u_r\boldsymbol{e}_r + u_\theta\boldsymbol{e}_\theta), \tag{19}$$

where $\boldsymbol{e}_r$ and $\boldsymbol{e}_\theta$ are unit vectors along the positive r and θ directions. Furthermore, $\boldsymbol{n}$ is the outer unit normal vector on the interface S_2, and Z_w and Z_l are specific acoustic impedances for the longitudinal waves in the water and lens, respectively. They are given by $Z_w = \rho c$ and $Z_l = \rho_0 c_l$. To obtain the total sound field behind the lens, we employ the Rayleigh integral associated with the velocity component v_n (the Rayleigh integral is not strictly valid for predicting a sound field emitted from a curved surface).

$$\phi = \frac{1}{2\pi}\iint_{S_0} v_n\frac{\mathrm{e}^{-\mathrm{j}kR}}{R}\,\mathrm{d}S. \tag{20}$$

Here, R is the distance between the source point Q on the interface S_2 and the receiving point P, and S_0 is the exit surface area.

3. Numerical examples

For comparison with the experimental data described below, we assign the dimensions of a PMMA lens, as listed in Table I.

The curvature radii d_1 and d_2 are both 60 mm, and the lens thickness h is 2 mm (hereinafter called simply the '60/60-mm lens'). The frequency of an incoming wave is 1 MHz. The table also indicates physical quantities necessary for numerical computation. We measured wave speed and sound absorption in PMMA at a frequency of 1 MHz and room temperature, using longitudinal and shear-wave transducers in direct contact with PMMA plates of different thicknesses in a through-transmission experiment. The obtained values were similar to data in the literature [7, 8, 9]. We set the lens aperture radius a at 37.5 mm under the constraint that waves impinging on the lens would be confined within the critical angle θ_c. The angle, defined as $\theta_c = \sin^{-1}(c/c_l)$, is 32.5°; thus, a is greater than $d_1 \sin\theta_c = 32.2$ mm (see Appendix A2).

Because of the relatively great sound absorption in the lens, we must modify our theory. Fortunately, we can accomplish this by introducing the complex wave numbers of $k_l = \omega/c_l - j\alpha_l$ and $k_t = \omega/c_t - j\alpha_t$ in place of $k_l = \omega/c_l$ and $k_t = \omega/c_t$ in equations (9) and (10).

The solid curve in Figure 2a is the pressure-amplitude profile along the beam. The abscissa denotes the axial distance beginning at the lens center 0, which is indicated in Figure 1. The ordinate denotes the pressure amplitude relative to the incoming pressure amplitude $|p| = |\mathrm{j}\omega\rho\phi_i| = \omega\rho$. This relative amplitude corresponds to the focusing gain. Apparently, the wave is focused by the lens effect. The pressure amplitude increases with peaks and dips during propagation, attains a maximum value of about 25 dB at the focus, and then decreases gradually. According to the thin-lens theory and paraxial approximation, the focal length z_f is given as

$$\frac{1}{z_\mathrm{f}} = (1 - n_\mathrm{r})\left(\frac{1}{d_1} + \frac{1}{d_2}\right), \tag{21}$$

where n_r is the reflection index defined as c/c_l, which is 0.537. Substituting this value and $d_1 = d_2 = 60$ mm into equation (21) results in $z_\mathrm{f} = 64.8$ mm.

Our lens model does not necessarily obey the thin-lens theory. The pressure actually peaks at 52 mm, about 13 mm less than the distance obtained from equation (21). In the figure, we performed a numerical calculation for the condition where all absorptions of longitudinal and shear waves are excluded, and the obtained results are denoted by dots. As we expect, the inclusion of the absorptions smooths out the rugged curve with its peaks and dips in the pre-focal and post-focal regions. Additionally, the propagation curves obtained when the generation of the shear wave is neglected by setting all the coefficients C_n and μ to be zero are denoted by dot-dashes. In contrast with the solid curve, the amplitude decreases monotonically in the post-focal region. More importantly, as previously indicated by other researchers, the shear wave does not markedly affect the field formation near the focus [3, 4, 5]. It, however, affects the field formation in the pre-focal and post-focal regions more significantly than that near the focus, within the specific framework of the present numerical examples.

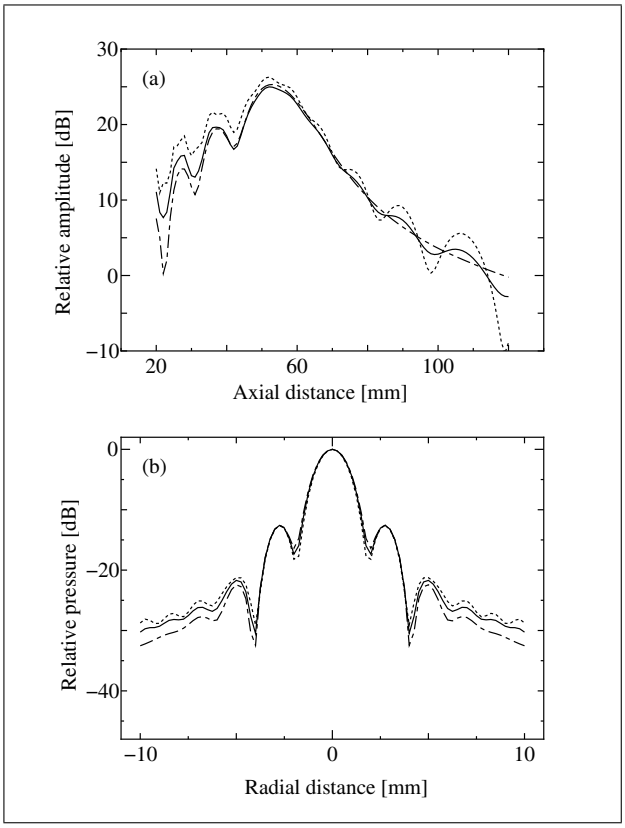

Figure 2. On-axis pressure amplitude, normalized to the incoming pressure $|p| = \omega\rho$ (a), for the 60/60-mm lens (solid curve) and its beam patterns at 52 mm in the focal plane (b). The data obtained when we ignored the generation of the shear wave are denoted by dot-dash lines. Dotted curves denote the pressure obtained when we excluded the absorption of all sounds in the lens.

Figure 2b shows the beam patterns in the focal plane at $z = 52$ mm. The patterns, particularly those of the main lobe and first side lobe, are almost independent of the inclusion of the generation of the shear wave and the sound absorption. Differences are found only in ranges greater than a distance of 5 mm from the beam axis. As exhibited by the ray trace in Appendix A1.1, a spherical aberration should appear in the patterns, suppressing insufficiently side-lobe levels. In fact, the first-lobe level is only −12.5 dB lower than the main-lobe level.

4. Experiments

We carried out experiments in a plastic tank (25 cm wide, 25 cm high, and 70 cm long) filled with degassed water. It is difficult to fulfill the conditions for plane-wave propagation in such a small tank. We therefore extended the theory to conditions where sound beams emitted from a piston source with a circular aperture are normally incident on the lens.

Using notations in Figure 3, a point source of sound on the aperture face S is expressed as

$$\frac{\mathrm{e}^{-\mathrm{j}kR}}{R} = -\mathrm{j}k \sum_{n=0}^{\infty} (2n+1) j_n(kr_1) h_n^{(2)}(kr_0) P_n(\cos\Gamma), \tag{22}$$

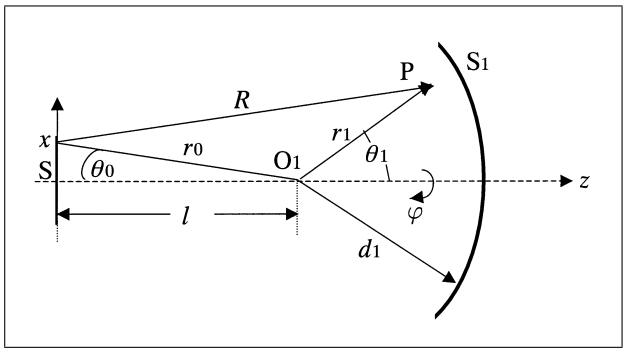

Figure 3. Theoretical model for a point source.

where $r_0 < r_1$ is required. $j_n(\cdot)$ and $h_n(\cdot)$ must interchange when $r_0 \geq r_1$. $P_n(\cos\Gamma)$ in equation (22) is given by

$$\begin{aligned} P_n(\cos\Gamma) &= \\ &P_n\left[\cos(\pi-\theta_0)\cos\theta_1 + \sin(\pi-\theta_0)\sin\theta_1\cos\varphi_0\right] \\ &= P_n(-\cos\theta_0)P_n(\cos\theta_1) + 2\sum_{m=1}^{n}(-1)^m P_n^m(-\cos\theta_0) \\ &\cdot P_n^{-m}(\cos\theta_1)\cos m\varphi_0, \end{aligned} \tag{23}$$

where φ_0 is the colatitude angle in the source plane and $P_n^m(\cdot)$ is the associated Legendre function of the first kind. Substituting equation (22) into the Rayleigh integral equation (20) reduces to the incident wave for the sound source. In the equation, the surface area element $\mathrm{d}S$ is $x\,\mathrm{d}x\,\mathrm{d}\varphi_0$ and the normal particle velocity v_n is approximated by $p_0/\rho c$, where p_0 is the source pressure amplitude. When performing the integration over the aperture face S, the second term in equation (23) vanishes in integrating from 0 to 2π with respect to φ_0. Then, equation (22) becomes finally equivalent to

$$\begin{aligned} \frac{\mathrm{e}^{-\mathrm{j}kR}}{R} &= -\mathrm{j}k\sum_{n=0}^{\infty}(2n+1)(-1)^n j_n(kr_1)h_n^{(2)}(kr_0) \\ &\cdot P_n(\cos\theta_0)P_n(\cos\theta_1). \end{aligned} \tag{24}$$

Replacing equation (6) with equation (24), multiplying $(p_0/\rho c)x\,\mathrm{d}x$, and integrating from 0 to the aperture radius of the source with respect to x, we can obtain the focused fields for the directive beam through the lens.

The sound source we employed was a planar ultrasound transducer with a circular aperture of 9.5 mm nominal radius and a resonance frequency of 1 MHz. The transducer was flush-mounted on the side-wall of the tank and was driven by a power amplifier. Electric tone-burst signals with a frequency of 1 MHz and a duration of 50 cycles were fed from a function generator. To detect a local sound pressure as precisely as possible, we used a needle-type hydrophone with an active diameter of 0.5 mm, which was mounted on a reliable translation stage driven by stepping motors. The motors enabled the stage to move precisely along and across the beam axis in steps of as small as 1 μm.

Figure 4a presents the sound pressure amplitudes along and across the beam axis with theoretical predictions based on the Rayleigh integral. We normalized all pressure data to the peak amplitude. In the theory, the source pressure amplitude p_0 was assumed to be distributed uniformly over the aperture face. Notable discrepancies occurred within ranges of less than 4 cm. We believe that such discrepancies are due to the non-uniformity of the amplitude on the source face. In contrast, they are in good agreement in the far field beyond the peak position at 5 cm away from the source. We estimated p_0 to be 40 kPa by the best fit of the experiment and theory in the far field, and determined that the active radius of the transducer is 9.4 mm.

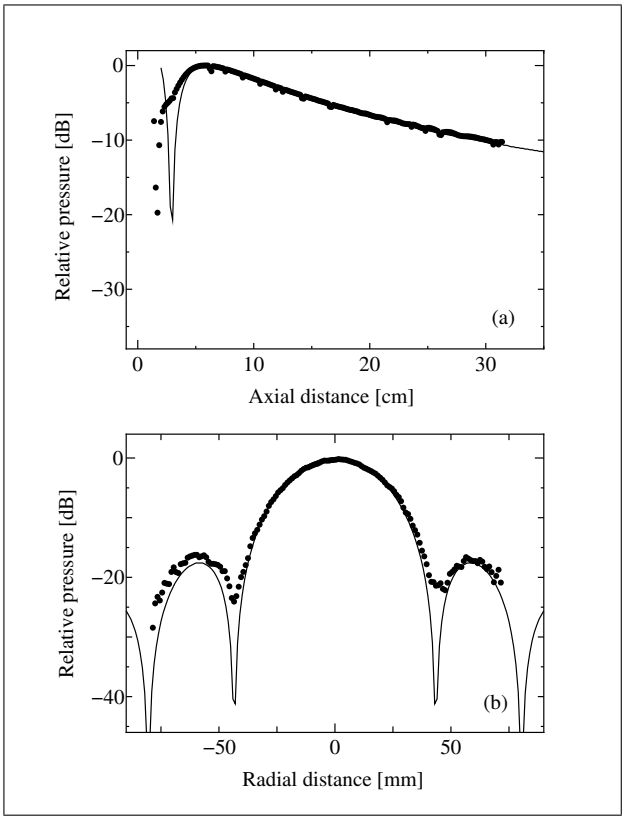

Figure 4. Propagation pressure curves (a) and beam patterns at 45 cm (b) for sound beams emitted from a 1-MHz planar transducer with a circular aperture of 9.5 mm radius: •, experimental data; —, theoretical predictions based on the Rayleigh integral. All the data are normalized to the peak amplitude.

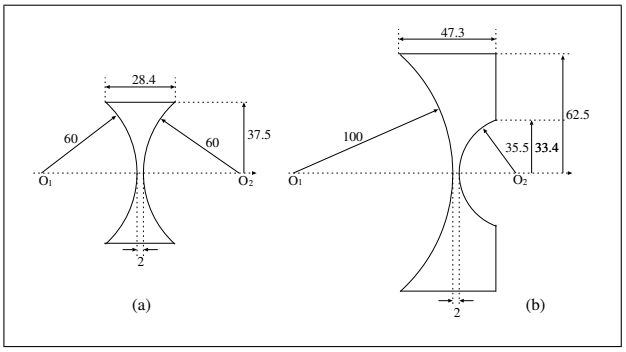

Figure 5. Cross sectional views of lenses: 60/60-mm lens (a) and 100/35.5-mm lens (b) used in the present experiment. Unit: mm.

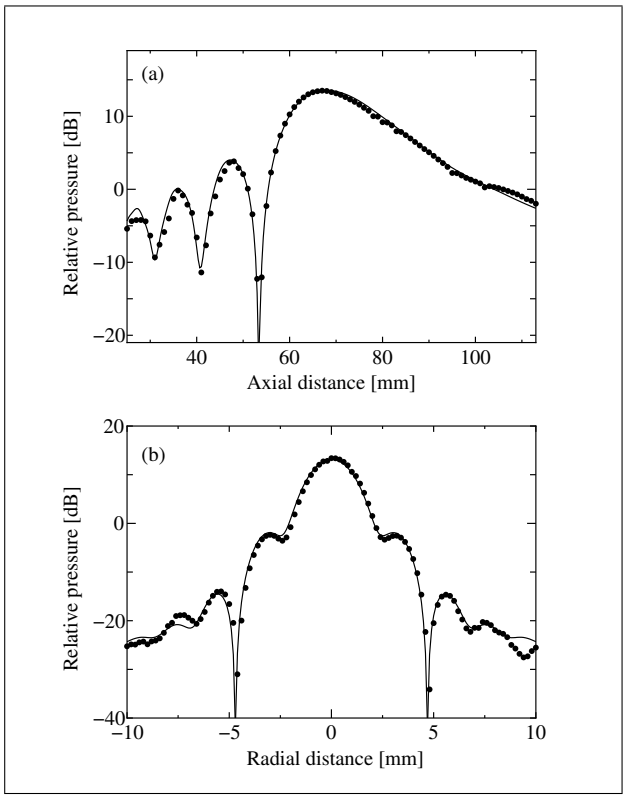

Figure 6. Axial pressure amplitude profiles a) and the beam patterns at $z = 64$ mm for the 60/60-mm lens (•: experiment; —-: theory). All the data are normalized to $p_0 = 40$ kPa.

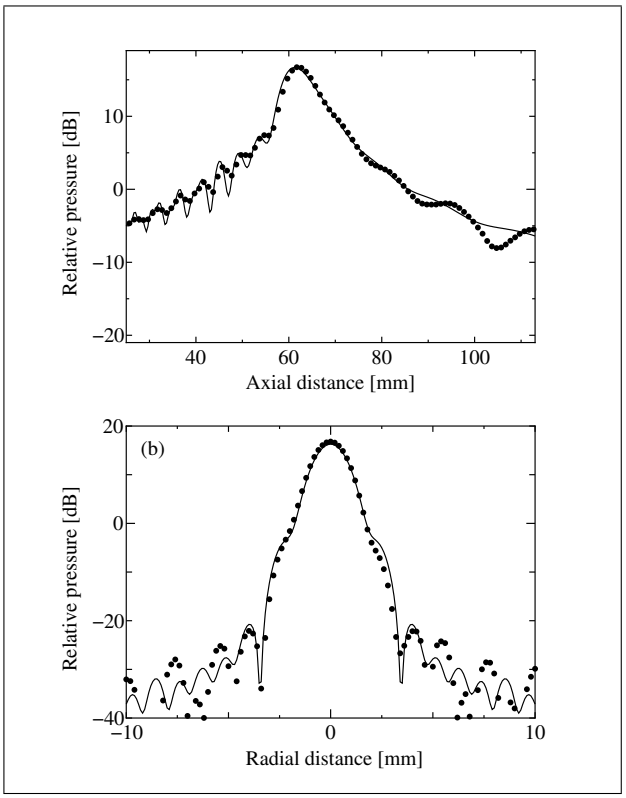

Figure 7. Axial pressure-amplitude profiles a) and beam patterns at $z = 61$ mm for the 100/35.5-mm lens (•: experiment; —-: theory). The dot-dash curve in a) indicates theoretical data, ignoring the generation of shear waves. All the data are normalized to $p_0 = 40$ kPa.

Figure 4b shows beam patterns at 45 cm, where acoustic lenses should be placed. The theoretical pattern is subject to the source radius being 9.4 mm. This pattern agrees with the experimental pattern except near the dips where noises arising from the hydrophone prevail against pressure signals.

For the experiment, we prepared two biconcave lenses made of PMMA. One is the 60/60-mm lens and the other is the 100/35.5-mm lens. The latter is designed to reduce the spherical aberration that occurs significantly in wide-aperture lenses and is responsible for image blurring. The effects of this aberration on lens performance chacteristics generally appear in beam patterns with high side-lobe levels and at a low focusing gain.

The cross-sectional views of both the lenses are illustrated in Figure 5. The focal lengths of the lenses that are almost identical are 50 mm (see Appendix A2). As already stated, the half-aperture angle of the 60/60-mm lens is also larger than the critical angle $\theta_c = 32.5°$. For the 100/35.5-mm lens, the half aperture angle is $\sin^{-1}(62.5/100) = 38.6°$, which is also larger than θ_c.

When measuring focused fields, we submerged the lens at 45 cm away from the transducer so that its centerline would coincide with the beam axis. At this lens location, the aperture of the 60/60-mm lens is almost the same as the width of the main lobe. For the 100/35.5-mm lens, the aperture contains the most part of the main lobe and first side lobe of the beam.

A quantitative comparison of the experiment and theory is shown in Figure 6 for the 60/60-mm lens with respect to pressure-amplitude profiles along and across the beam axis, in which the pressure amplitudes in the ordinates are relative to the expected source-pressure amplitude $p_0 = 40$ kPa. The agreement between both data sets is excellent as a whole. The peak pressure is 14 dB, which is attained at 64 mm from the lens. The width of the focal region, here defined as 6 dB below from the peak magnitude, is 26 mm. In comparison with Figure 2, the peak position is 12 mm away from the focus because the wave front of the incident beam is more likely spherical than planar.

Additionally, the beam patterns in the focal plane are slightly different from those in Figure 2b: the dips at ±2 mm from the beam axis almost disappear for the directive beam in Figure 6b.

We measured the on-axis pressure amplitudes for the 100/35.5-mm lens in the same manner. The data are shown in Figure 7a. The peak pressure is 17 dB, which is 3 dB higher than that of the 60/60-mm lens. The focal region is almost half of the width, 11 mm.

Interestingly, the propagation profiles are devoid of acute peaks and dips in the pre-focal region, unlike the distinct oscillation of the 60/60 mm-lens. In the post-focal region, however, we find a few peaks and dips within the observation range of less than 125 mm, although the theoretical curve does not exhibit such large changes.

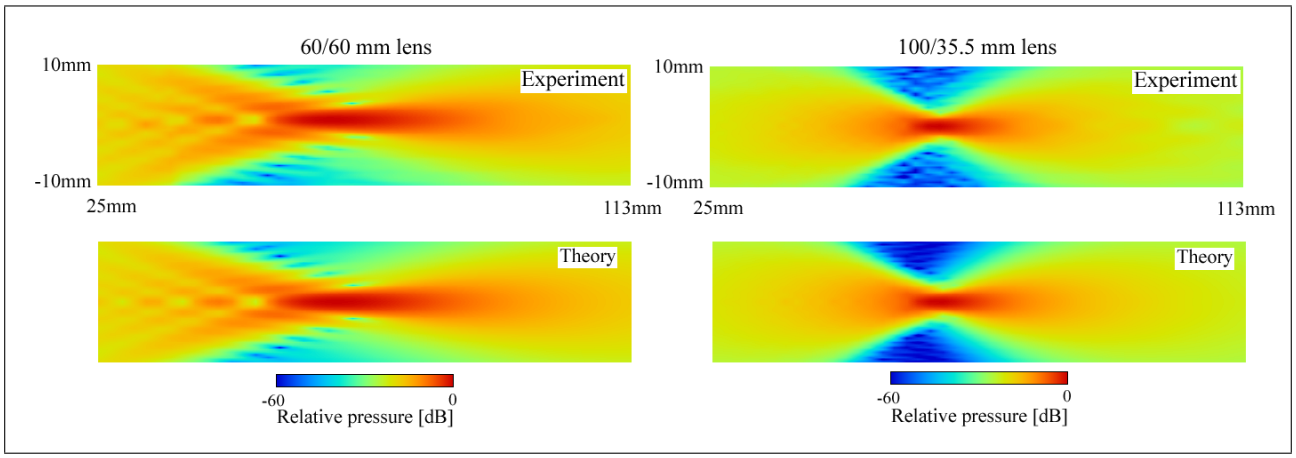

Figure 8. Comparison of measured (upper) and calculated (lower) pressure distributions in the $r - z$ plane. Data for the 60/60-mm lens (left) and 100/35.5-mm lens (right).

The theory does not accurately predict the oscillatory structure of side lobes at 5 mm or more from the beam axis for the beam patterns in Figure 7b. The potential source of such oscillation seems to be the multiple wave reflections in the lens that have been ignored in the present theory. The simplified boundary conditions given by equations (18) and (19) might be another source. At any rate, it should be noted that the pressure of the first side lobe for the 100/35.5-mm lens is more than 20 dB lower than that for the 60/60-mm lens.

We moved the hydrophone from -10 to 10 mm in the r direction at intervals of 0.4 mm, and from 25 to 113 mm in the z direction at intervals of 2 mm. The thus obtained pressure distributions in the $r - z$ plane including the focus are shown in Figure 8 as two-dimensional views. As in Figure 6, the excellent agreement between the theory and the experiment is also noted for the 60/60-mm lens. The beam achieved by the 100/35.5-mm lens narrows quickly with axial distance, and then abruptly spreads out after passing through the focus. Alternating dark and light colors in blue, which intrinsically have the same appearance in the small side lobes in Figure 7b, are observed in the measured distributions.

5. Comments on the hybrid method

As described in Introduction, the hybrid method that incorporates the concepts of geometric acoustics in the lens and wave acoustics in an image space behind the final lens surface has been used as a predictor in a sonar imaging system. Undoubtedly, the hybrid method is simple in concept and powerful in usage because it is readily applicable to the analysis of fields achieved by a single lens and a multilens system. Such simplicity and applicability are of importance in designing lenses before fabrication. It is also of considerable importance to know whether the hybrid method can describe accurately the fields, as expected. From this perspective, it is interesting to compare the present wave theory with the hybrid method using the same lens model.

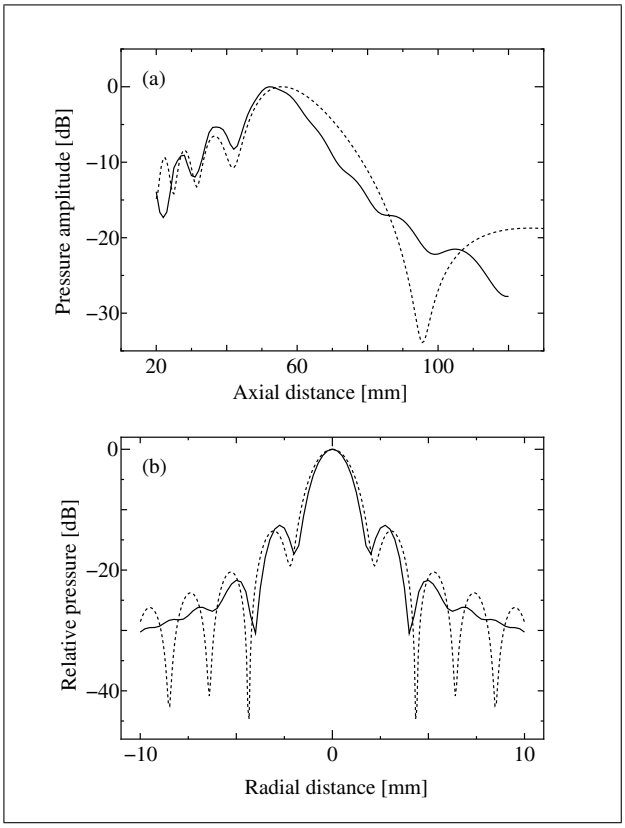

Figure 9. Comparison of the pressure distributions between the present wave theory (solid) and the hybrid method (dotted) for the 60/60-mm lens. The upper figure (a) presents the propagation curves along the beam axis and the lower figure (b) the beam patterns at $z = 53$ mm (present theory) and $z = 55$ mm (hybrid method). All the data are normalized to the peak amplitude.

Sound pressure distributions for the case of a 1-MHz plane wave incidence on the 60/60-mm lens are presented in Figure 9. The data obtained using the wave theory are indicated by solid curves; these data are essentially the same as those in Figure 2 except for the pressure peaks being normalized to unity in the ordinates. The data obtained

by the hybrid method are indicated by dotted curves. Figure 9a shows on-axis pressure curves. As can be seen, both theoretical curves exhibit almost similar increases with peaks and dips in the pre-focal region. However, the positions of the pressure peak, the foci, are somewhat different; i.e., the focus exists at $z = 55$ mm, which is by 2 mm away from the focus predicted by the wave theory. In addition, the focal region is broader than that predicted using the wave theory. In the post-focal region, a significant difference is discernible as the first dip appearance at 95 mm, which is not seen in our wave theory.

Figure 9b shows beam patterns across the beam axis at the pressure peaks; i.e., at $z = 53$ mm for the present theory and $z = 55$ mm for the hybrid method. Generally, a negligible broadeness is seen for the patterns predicted by the hybrid method. Besides, side lobe levels are estimated to be slightly lower than those obtained using the present wave theory. Although numerical demonstrations are limited to a single lens and a normal incident case, it is expected that the hybrid method is a crude predictor for describing sound propagation around the focus and an almost satisfactory predictor for describing beam patterns in the focal plane.

Incidentally, the resolution power of a circular lens is ultimately determined by the Rayleigh's criterion [10], that says for the angular width as

$$\Delta\theta = 1.22\frac{\lambda}{2a}, \tag{25}$$

where λ is the wavelength and a is the radius of the lens aperture. Provided that the aperture radius is confined by the critical angle θ_c, $a = 32.2$ mm because a is given by $d \sin\theta_c$. In this case, then, $\Delta\theta$ takes a value of 1.6°. On the contrary, the actual angular width is $\Delta\theta = 1.9$ mm/53 mm = 2.1° from Figure 9b. The obvious reason why the difference of 0.5° appears is due to the spherical aberration that leads to the primary responsibility for image blurring. The aberration is ordinarily reduced by making a lens aperture small and/or by use of an aspherical lens.

6. Conclusions

In this study, we theoretically and experimentally investigated the focusing of ultrasonic waves using acoustic lenses submerged in water. We treated plane and directive waves to be normally incident on the lenses, which were made of PMMA and were spherically biconcave. We based our theoretical approach on the expansion of incident waves into spherical waves to satisfy boundary conditions conveniently. This theoretical approarch demonstrated both the shear wave generation and sound absorption in the lens affecting focused fields in the pre-focal and post-focal regions, rather than those near the focus. Using a 1-MHz ultrasound transducer with a circular aperture of 9.5 mm radius, we measured focused fields for two lenses with curvature radii of 60/60 mm and 100/35.5 mm. The excellent agreement between the theory and the experiment supported the validity of our theory. Additionally, we determined the applicability of the hybrid method, which is used in designing lenses, to our lens model.

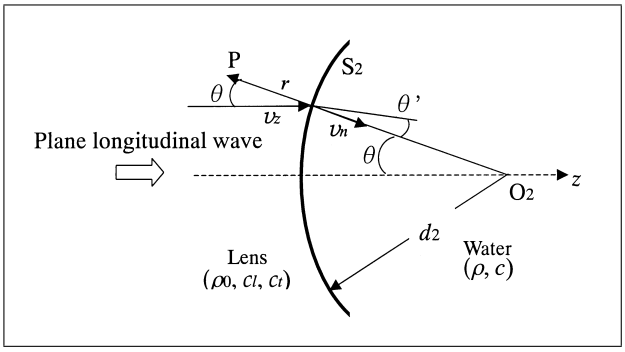

Figure A1. Model of a spherical concave lens. A longitudinal plane wave is assumed to be incident on the lens surface S_2.

Appendix A1

The wave front in the lens is not plane in nature. However, we consider the special situation where a plane longitudinal wave is incident on the spherical curved surface S_2 for theoretical simplicity. The lens model with the exit surface is shown again in Figure A1. The longitudinal displacement potential $\psi_i = e^{jk_l r\cos\theta}$ can be expanded into spherical waves in the same manner as the theoretical development in the present body [11]:

$$\psi_i = \sum_{n=0}^{\infty} j^n(2n+1)j_n(kr)P_n(\cos\theta). \tag{A1}$$

The reflected longitudinal wave ψ_r and shear wave A_φ from the surface, and the transmitted longitudinal wave ϕ are also written as

$$\left.\begin{aligned}
\psi_r &= \sum_{n=0}^{\infty} A_n j^n(2n+1)h_n^{(2)}(k_l r)P_n(\cos\theta)\\
A_\varphi &= \sum_{n=0}^{\infty} B_n j^n(2n+1)h_n^{(2)}(k_t r)\frac{\mathrm{d}}{\mathrm{d}\theta}P_n(\cos\theta)\\
\phi &= \sum_{n=0}^{\infty} C_n j^n(2n+1)h_n^{(1)}(kr)P_n(\cos\theta)
\end{aligned}\right\}, \tag{A2}$$

where the three coefficients A_n, B_n, and C_n are determined under the appropriate boundary conditions of the displacement and stress on the surface at $r = d_2$.

The transmission coefficient of the particle velocity T_v ($= |T_v|e^{j\beta}$), which is defined here as the ratio of the normal component of the transmitted wave v_n ($= \partial\phi/\partial r|_{r=d_2}$) to the z component of the incident wave v_z ($= \partial\psi/\partial t = j\omega e^{jkd_2\cos\theta}$), is obtained using the above-mentioned equations. The numerical results are shown by solid curves in Figure A2. Lens parameters are the same as those in Table I. The curvature radius d is 60 mm.

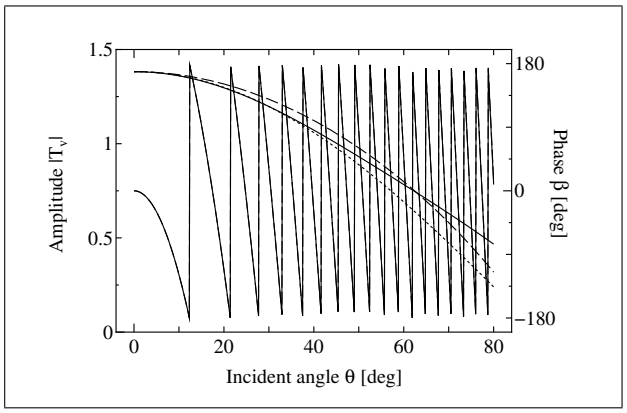

Figure A2. Magnitudes and phases of the transmission coefficient of the particle velocity. Solid curves: equations (A1) and (A2); dashed curves: equation (A3); dotted curve: equation (A5). The phase β begins with 0° at $\theta = 0°$. The β data obtained using equation (A3) overlap completely with those obtained using the wave theory. $|T_v|$ is determined to be 1.38 at $\theta = 0$ by substituting $Z_l = 3.26\times10^6$ Ns/m^3 and $Z_w = 1.48\times10^6$ Ns/m^3 into equation (A5).

If the curvature radius is much larger than the wavelength, the following two simple formulas must hold approximately. One is the well-known expression that is derived for the case where a plane wave is obliquely incident at a plane interface between two different fluids [12]:

$$|T_v| = \frac{2Z_l \cos\theta}{Z_l \cos\theta' + Z_w \cos\theta} \cos\theta', \qquad \beta = -k_l d(1-\cos\theta), \tag{A3}$$

where θ' is the angle between the transmitted ray and the normal axis, being determined by the following Snell's law:

$$\frac{\sin\theta}{c_l} = \frac{\sin\theta'}{c}. \tag{A4}$$

$|T_v|$ and β are denoted by dashed curves in Figure A2, where the β data overlap entirely with the data obtained using equation (A2). We propose here a more simple expression for the transmission coefficient by neglecting Snell's law

$$|T_v| = \frac{2Z_l}{Z_l + Z_w} \cos\theta. \tag{A5}$$

The expression for the phase β is the same as that in equation (A3). The data obtained using this equation are denoted by dots in Figure A2. In comparison with the wave theory that seems to be an accurate predictor, the data obtained using equation (A5) are not so different in magnitude within a wide range of incidence angle, e.g., less than 40°. Actually, the incidence angles of the rays on the surface S_2 seem not to exceed 40°, as indicated in the next Appendix A2. Thus, the simple expressions for $|T_v|$ and β, equations (A3) and (A5), must be useful for describing the particle velocity component v_n.

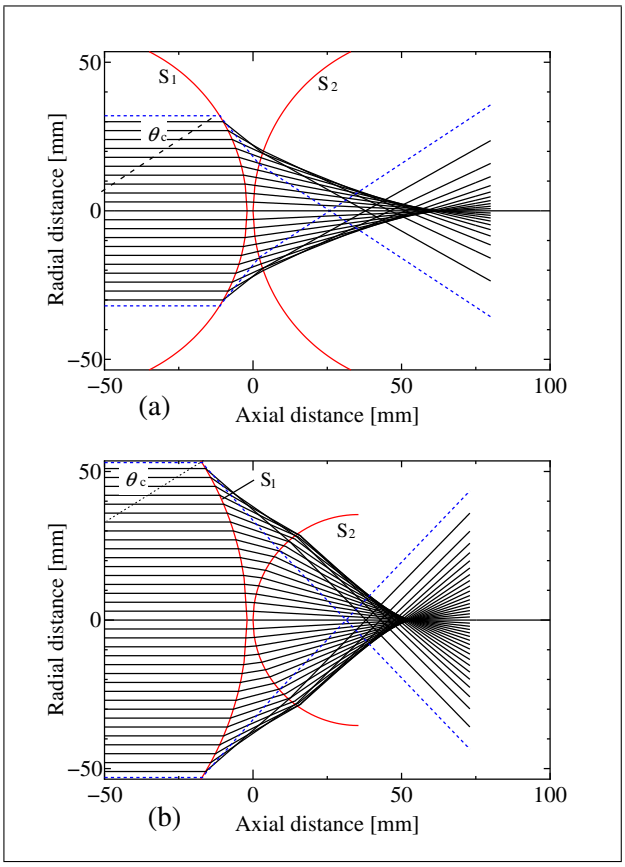

Figure A3. Ray tracing for two lenses. a) $d_1 = 60$ mm and $d_2 = 60$ mm, b) $d_1 = 100$ mm and $d_2 = 35.5$ mm. Dotted curves denote the rays at 32°, immediately before the critical angle θ_c of 32.5°.

Appendix A2

We apply the geometric ray theory to the present biconcave lens model. Figure B shows the propagation trajectory of each ray in accordance with Snell's law. θ_c is the critical angle of a refracted ray along the water/lens interface, having an angle of refraction of 90 degrees. This angle is determined to be $\sin^{-1}(c/c_l) = 32.5°$. None of the rays with incidence angles exceeding θ_c penetrate the lens. As we observe in Figure A3a, the rays seem to be concentrated near 50 mm, nearly the same position as that predicted from wave acoustics (Figure 2a). Additionally, the rays produced by the 100/35.5-mm lens are more concentrated than those produced by the 60/60-mm lens.

Acknowledgement

The authors are grateful to Hiroshi Uchiyama, a postgraduate student of the University of Electro-Communications, for his assistance with experiments. The present work is partially supported by the Ministry of Education, Culture, Sports, Science and Technology, through a Grant-in-Aid for Exploratory Research, 16656062, and by the Mitsubishi Electric Corporation.

References

[1] K. Fink: Computer simulation of pressure fields generated by acoustic lens beamformers. Master thesis of The University of Washington, 1994.

[2] T. Kamakura, K. Aoki, T. Nakamura, H. Adachi: Focusing of a plane ultrasonic wave by a bi-concave lens – Theoretical approach. J. Marine Acoust. Soc. Jpn. **30** (2003) 48–57.

[3] D. L. Folds, J. Hanlin: Focusing properties of a solid four-element ultrasonic lens. J. Acoust. Soc. Amer. **58** (1975) 72–77.

[4] H. W. Jones, C. J. Williams: Lenses and ultrasonic imaging. – In: Acoustical Holography. L. W. Kesseler (ed.). Plenum, New York, 1977, 133–153.

[5] H. W. Jones, H. W. Kwan: Ultrasonic lenses for imaging. Ultrasonics **23** (1985) 63–70.

[6] T. Nakamura, Y. Sato, T. Kamakura, T. Anada: Sound pressure fields focused using biconcave acoustic lens for normal incidence. Jpn. J. Appl. Phys. **43** (2004) 3163–3168.

[7] B. Hartmann, J. Jarzynski: Ultrasonic hysteresis absorption in polymers. J. Appl. Phys. **43** (1972) 4304–4312.

[8] E. Juliac, J. Arman, D. Harran: Ultrasonic interferences in polymer plates. J. Acoust. Soc. Amer. **104** (1998) 1232–1241.

[9] Y. Bouzidi, D. R. Schmitt: A large ultrasonic bounded acoustic pulse transducer for acoustic transmission goniometry: Modeling and calibration. J. Acoust. Soc. Amer. **119** (2006) 54–64.

[10] W. C. Elmore, M. A. Heald: Physics of waves. Dover Publications, New York, 1985. Sec. 10.4.

[11] M. Akiyama, H. Uchiyama, T. Kamakura: Focused sound beams by an elliptic surface lens. J. Acoust. Soc. Jpn. **61** (2005) 71–78.

[12] D. T. Blackstock: Fundamentals of physical acoustics. John Wiley & Sons, New York, 2000. Chap. 5.